AGU PUBLICATIONS

JGR

Journal of Geophysical Research: Solid Earth

RESEARCH ARTICLE
10.1002/2014JB011036

Key Points:
- We simulated pressure solution creep of random packs of spheres
- Simulated strain rates not well described by common constitutive laws
- Results similar to experiments closely resembling our simulations

Correspondence to:
Y. Bernabé,
yvb@mit.edu

Citation:
Bernabé, Y., and B. Evans (2014), Pressure solution creep of random packs of spheres, *J. Geophys. Res. Solid Earth*, *119*, 4202–4218, doi:10.1002/2014JB011036.

Received 10 FEB 2014
Accepted 29 APR 2014
Accepted article online 4 MAY 2014
Published online 27 MAY 2014

Pressure solution creep of random packs of spheres

Y. Bernabé[1] and B. Evans[1]

[1]Earth, Atmospheric and Planetary Sciences Department, Massachusetts Institute of Technology, Cambridge, Massachusetts, USA

Abstract We performed numerical calculations of compaction in aggregates of spherical grains, using Lehner and Leroy's (2004, hereinafter LL) constitutive model of pressure solution at grain contacts. That model is founded on a local definition of the thermodynamic driving force and leads to a fully coupled formulation of elastic deformation, dissolution, and diffusive transport along the grain boundaries. The initial geometry of the aggregate was generated by random packing of spheres with a small standard deviation of the diameters. During the simulations, isostatic loading was applied. The elastic displacements at the contacts were calculated according to Digby's (1981) nonlinear contact force model, and deformation by dissolution was evaluated using the LL formulation. The aggregate strain and porosity were tracked as a function of time for fixed temperature, applied effective pressure, and grain size. We also monitored values of the average and standard deviation of total load at each contact, the coordination number for packing, and the statistics of the contact dimensions. Because the simulations explicitly exclude processes such as fracturing, plastic flow, and transport owing to surface curvature, they can be used to test the influence of relative changes in the kinetics of dissolution and diffusion processes caused by contact growth and packing rearrangements. We found that the simulated strain data could be empirically fitted by two successive power laws of the form, $\varepsilon_x \propto t^{\xi}$, where ξ was equal to 1 at very early times, but dropped to as low as 0.3 at longer times. The apparent sensitivity of strain rate to stress found in the simulations was much lower than predicted from constitutive laws that assume a single dominant process driven by average macroscopic loads. Likewise, the apparent activation enthalpy obtained from the simulated data was intermediate between that assumed for dissolution and diffusion, and, further, tended to decrease with time. These results are similar to the experimental observations of Visser et al.'s (2012), who used an aggregate geometry and physical conditions closely resembling the present numerical simulations.

1. Introduction

Geological evidence indicates that pressure solution (PS), i.e., granular flow accommodated by transfer of matter via an interstitial solvent fluid (usually an aqueous solution), is an important deformation mechanism in the upper crust [e.g., *Rutter*, 1983; *Gratier*, 1987; *Tada and Siever*, 1989]. Among other things, PS creep is thought to affect fault gouge healing during the interseismic period [e.g., *Blanpied et al.*, 1992; *Hickman and Evans*, 1992; *Segall and Rice*, 1995; *Fitzenz et al.*, 2007] and to be important in reducing porosity with depth in sedimentary basins (for discussions, see *Renard et al.* [2000], *Revil* [2001], and *Ehrenberg et al.* [2009]).

Early theoretical analyses of PS [e.g., *Weyl*, 1959; *Paterson*, 1973, 1995; *Rutter*, 1976; *Raj*, 1982] rest on several elementary assumptions: (1) a thin, dynamically stable, fluid-saturated interface capable of transmitting arbitrary tractions from grain to grain must exist at the grain contacts; (2) PS is a compound process combining four elementary mechanisms, namely, dissolution at stressed grain contacts, diffusive transport in the fluid saturating the contact interfaces, diffusive/advective transport in the pore space outside the contact interface, and deposition on the free surface of grains; (3) these mechanisms are acting in series and the slowest one is therefore rate limiting; and (4) the transfer of matter is thermodynamically forced by the global difference in chemical potential between the sources and sinks. The earliest models resulted in constitutive relations, in which strain rates were related linearly to the effective pressure and inversely to grain size raised to a power between 1 and 3, although later refinements have produced relations with more complicated systematics [e.g., *Spiers et al.*, 1990; *Revil*, 1999; *Renard et al.*, 2000; *Niemeijer et al.*, 2002; *Dysthe et al.*, 2002; *Gratier et al.*, 2009; *Taron and Elsworth*, 2010]. Nearly all of these elementary assumptions have been the subject of debate, but the structure of the contact interface has been a topic of particularly great interest. Proposals include strongly adsorbed water films [e.g., *Weyl*, 1959; *Rutter*, 1983; *Renard and Ortoleva*, 1997], a dynamic island-channel structure [e.g., *Raj*, 1982; *Lehner*, 1990; *Paterson*, 1995], microcracks [e.g., *Gratz*, 1991; *den Brok*, 1998], or a thin layer of hydrated gel [*Revil*, 2001].

More often overlooked, but still important to examine are the assumption of serial coupling of the elementary mechanisms and the reliance on a macroscopic, averaged chemical potential gradient as the thermodynamic driving force. *Lehner and Bataille* [1984/1985], *Lehner* [1990, 1995], and *Lehner and Leroy* [2004, hereinafter LL] have developed a more physically accurate formulation that considers the local jump in chemical potential, $\mu_s(\boldsymbol{x}) - \mu_f(\boldsymbol{x})$, where μ_s and μ_f refer to the chemical potentials in the solid and fluid, respectively; here, $\boldsymbol{x}$ denotes the location of a particular infinitesimal volume traversing the solid-fluid interface either at the free surface of the grains or within the grain contact. Either dissolution or precipitation may occur, depending on the sign of the chemical potential jump. Concurrently, solid matter is transferred by diffusion from high to low μ_s regions, i.e., from the sources to the sinks. In Lehner's formulation, the chemical potentials μ_f and μ_s are given as functions of space and time:

$$\mu_f(\boldsymbol{x},t) - \mu_0 = \frac{kT}{\rho_s \Omega_s} \ln\left(\frac{\gamma c(\boldsymbol{x},t)}{\gamma_0 c_0}\right) \tag{1}$$

and

$$\mu_s(\boldsymbol{x},t) - \mu_0 = \frac{\sigma_n(\boldsymbol{x},t) - p_f}{\rho_s} + (f(\boldsymbol{x},t) - f_0), \tag{2}$$

where t denotes time, T the temperature, k the Boltzmann constant, ρ_s the solid density, Ω_s the molecular volume of the solid, σ_n the normal stress, p_f the fluid pressure, c the solute concentration in the saturating solution, γ the activity coefficient (assumed to be approximately constant so that the ratio γ/γ_0 can be removed from equation (1)), and f the Helmholtz free energy of the solid. The subscript 0 indicates the state of thermodynamic equilibrium of the solid saturated by a fluid at temperature T and fluid pressure p_f. Considering an individual grain contact and assuming that, at the contact scale, the interface can be described as a smooth, uniformly thin layer (with unspecified internal structure), it is usually admitted that the Helmholtz term in equation (2) is negligible compared to the normal stress term (for example, see LL).

In Lehner's formulation, the instantaneous mass flux of dissolved solid per unit surface area is the following:

$$J(\boldsymbol{x},t) = \rho_s K_s \left[\frac{\Omega_s}{kT}(\sigma_n(\boldsymbol{x},t) - p_f) - \ln\left(\frac{c(\boldsymbol{x},t)}{c_0}\right)\right], \tag{3}$$

where K_s is a phenomenological rate coefficient for dissolution at the contact surface. The diffusion of solute in the contact interface can then be calculated by plugging $J(\boldsymbol{x}, t)$ as a source term in the appropriate diffusion equation (e.g., quasi-static and two-dimensional if the contact interface is sufficiently thin):

$$\nabla^2 c(\boldsymbol{x},t) = \frac{\rho_s K_s}{\rho_f w D}\left[\frac{\Omega_s}{kT}(\sigma_n(\boldsymbol{x},t) - p_f) - \ln\left(\frac{c(\boldsymbol{x},t)}{c_0}\right)\right], \tag{4}$$

where ρ_f is the fluid density, w the thickness of the contact interface, and D the effective interface diffusion coefficient. To allow for uncertainty in the boundary diffusion coefficient, we include a retardation factor, $f_r < 1$, that accounts for the difference between the actual diffusion coefficient along the boundary, D, and the molecular diffusion coefficient in the pore fluid, D_m; thus, $D = f_r D_m$.

If the normal stress field is known, the flux and continuity equations (3)–(4) can be solved numerically to determine $c(\boldsymbol{x}, t)$ and $J(\boldsymbol{x}, t)$ [*Bernabé and Evans*, 2007, hereinafter BE]. From these calculations, one can obtain the thickness of the layer of solid dissolved at $\boldsymbol{x}$ during an infinitesimal interval of time δt. The amount of material removed during each time increment determines the change in shape of the contacting grains, from which the new stress field can be calculated using contact mechanics. Repeating this sequence gives the time evolution of an individual grain contact. For initially spherical quartz grains in normal contact, BE obtained decelerating convergence rates associated with contact growth, flattening of the contacting grains, and transfer of stress from the center of the contact to its periphery. Note that, because the source term on the right-hand side contains c, equation (4) is inconsistent with the general assumption that interface dissolution and diffusion are strictly sequential processes. Thus, the conditions, under which the PS kinetics are dominated by a single rate-limiting mechanism, are greatly reduced (see BE).

Experimental tests of pressure solution can be separated into classes characterized as single contact or multigrain (aggregate) tests. Single contact tests observe the evolution of individual fluid-saturated, solid-solid contacts of various geometries (in some cases, in real time under the microscope). For example, *Hickman and Evans* [1991, 1992, 1995] and *Dysthe et al.* [2002, 2003] pressed smooth, spherical, or cylindrical indenters

against flat substrates. The growth of the contacts and decelerating convergence rates observed in the tests were qualitatively similar to the BE numerical simulations. When sharp, rectangular, or conical indenters were used [*Tada and Siever*, 1986; *Gratier*, 1993; *Gratier et al.*, 2009; *Karcz et al.*, 2006, 2008], undercutting of the solid free surface near the highly stressed contact occurred, often in combination with microcracking or plastic yielding. See *Ghoussoub and Leroy* [2001] for numerical simulations of undercutting. Using other types of configurations, *de Meer et al.* [2002, 2005] performed clever experiments specifically designed to characterize the thickness and diffusive properties of stressed, fluid-saturated contact interfaces. One recurring observation is that convergence rates strongly increased when structural irregularities, including scratches, microcracks, or small-scale roughness of the solid surfaces, were present, when the substrate was a dissimilar mineral, or when the contact region contained a layer of clay particles.

Individual contact experiments often provide the opportunity for direct observation of the deformation mechanisms, but their results are not easy to generalize to natural crustal rocks containing a large number of grains of variable sizes and shapes. Thus, many workers have chosen to measure compaction creep of monomineralic or polymineralic granular aggregates [e.g., *Cox and Paterson*, 1991; *Spiers et al.*, 1990; *Schutjens*, 1991; *Rutter and Wanten*, 2000; *Renard et al.*, 2001; *Niemeijer et al.*, 2002, 2009; *Chester et al.*, 2004, 2007; *Zubtsov et al.*, 2004; *van Noort et al.*, 2008; *Visser et al.*, 2012]. However, the aggregate compaction experiments also have drawbacks. In particular, it is very difficult to prevent the occurrence of other (non-PS) processes, and it may be difficult to parse the effects of the individual mechanisms. For example, stress-corrosion microcracking was found to be dominant in experiments measuring compaction of fluid-filled quartz aggregates at relatively low temperature [*Chester et al.*, 2004, 2007]. Further, the number, sizes, and shapes of the grain contacts as well as their topology cannot be monitored during aggregate compaction experiments. High levels of grain heterogeneity (likely enhanced by grain comminution during the cold pressing stages of the experiments, e.g., *Revil et al.* [2006]) and packing disorder are expected to affect PS creep significantly. Calculations suggest that PS creep rates will decrease owing to stress transfer when the contacts involve grains of different curvature or when contacts are newly created [*Bernabé et al.*, 2009]. Changes in contact coordination number strongly affect both the densification rates of metal powders [*Arzt*, 1982] and the elastic properties of unconsolidated granular materials [*Makse et al.*, 1999; *Dutta et al.*, 2010].

In this paper, we present numerical calculations of compaction in an aggregate of spherical grains where PS occurs as described by Lehner's model. Because the computations include specific information on the grain configuration at any time, we can evaluate the magnitude of the effect of packing changes on compaction rate. Additionally, there is no ambiguity about which mechanisms operate, because these, too, are explicitly specified. Thus, we can use the simulations to assess the effects on the aggregate compaction rates when diffusion and dissolution are fully coupled at the microscopic scale and when packing geometry changes substantially. The initial configuration is generated by random packs of spheres, which are subjected to dry isostatic compression using the method of *Cundall and Strack* [1979]. We then compute compaction rates and the evolution of sphere configurations assuming that a solvent fluid fully saturates the pore space and allows PS to occur via Lehner's model. The simulations were performed for conditions of constant macroscopic effective pressure and temperature. We monitored contact coordination number, the contact force statistics, total porosity, and other relevant parameters.

2. Numerical Methods and Procedures

2.1. Numerical Granular Mechanics: Background

Since the pioneering work of *Cundall and Strack* [1979], numerical methods such as the Distinct Element Method (DEM) have been frequently used to tackle mechanics problems involving discontinuous solid bodies. Examples from among many applications include studies to gain insights into the micromechanical origin of the plastic behavior of soil [*Rothenburg and Kruyt*, 2004; *Gong*, 2008], to understand the effect of a cement phase [*Bruno and Nelson*, 1991; *Holtzman*, 2012], to model comminution of gouge during shear [*Mair and Abe*, 2008], to simulate hydraulic fracturing [*Boutt et al.*, 2007], or to simulate compaction of plastically strained aggregates [*Martin et al.*, 2003; *Uri et al.*, 2006; *Hartong et al.*, 2009].

At its core, DEM simply consists in applying Newton's laws of motion to a set of solid bodies that interact only through contact forces. The different variations reported in the literature correspond to peripheral (although important) details such as the shape of the solid grains, the contact interaction laws and/or the collision rules used when ballistic flight of the solid grains occurs. Here we opted for simplicity and considered

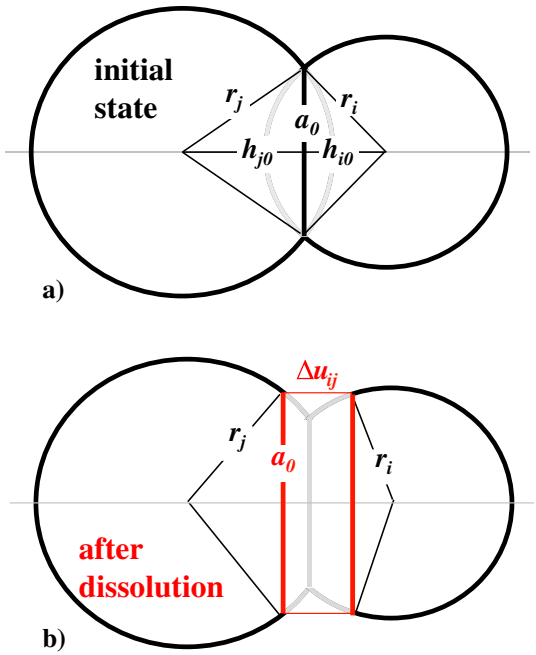

Figure 1. Schematic depictions of: (a) the cross section of two unstressed, contacting spheres of radii r_i and r_j. The unstressed interface has a radius a_0 and the distance between the centers at zero load is $h_0 = h_{i0} + h_{j0}$. (b) The cross section of the layers of dissolved solid along the contact interface. The red rectangle graphically defines the dissolution displacement Δu_{ij} and the radius a_0 of the postdissolution interface at zero stress.

indestructible, elastic, cohesionless, and frictionless spheres, which can deform inelastically only by pressure solution. Assumptions such as elasticity, absence of cohesion forces, and a spherical grain shape are commonly made in DEM studies of unconsolidated granular materials. Although friction plays an important role in real materials, there are some valuable advantages in omitting it in initial studies. Clearly, it is much easier to implement DEM when friction is absent and when only normal contact forces are considered. More importantly, the frictionless case is a useful benchmark. For example, irreversibility and loading history effects are known to arise in numerical simulations, despite the absence of friction or other dissipative mechanisms. This fact has important consequences on theoretical models of the mechanics of unconsolidated granular materials [e.g., *Roux*, 2000]. The use of frictionless grains was also found to be a good approximation for plastically deformed sphere packs, in which rotation of grains tend to be small [e.g., *Martin et al.*, 2003]. Likewise, omitting grain fracturing, despite its frequent occurrence in laboratory experiments, is justified when small spherical grains are considered and when the applied confining pressure is limited to an appropriate range. For example, *Karner et al.* [2003] measured a critical pressure of 107 MPa in St. Peter sand (well-rounded sand with a 150 μm grain diameter) and *Makse et al.* [2004] did not observe grain fracturing in glass beads (grain diameter = 45 μm) compressed up to 130 MPa. Therefore, for our simulations, we selected sphere diameters and effective confining pressures within this range (i.e., $2r = 80$ μm and $p_c \leq 120$ MPa).

In order to calculate the quasi-instantaneous response of dense sphere packs in mechanical equilibrium to increments of load or displacement, DEM can be efficiently used as an iterative relaxation method operating in virtual time with arbitrary grain masses and damping terms, adjusted to optimize the virtual time increment, $\delta\tau$, used in the calculations. The optimal value will minimize the number of iterations needed for the disturbed sphere pack to reach a new equilibrium state [e.g., *Martin et al.*, 2003]. *Cundall and Strack*'s [1979] guidelines for insuring numerical stability must, of course, be followed when adjusting $\delta\tau$. The iterative relaxation DEM appeared to be well suited for our purpose and was therefore implemented here.

Another important observation is that the results of DEM studies depend strongly on the procedures used to construct the initial, unstressed sphere packs [*Agnolin and Roux*, 2008]. Here we are interested in relatively dense, stiff sphere packs. We also wish to ensure a sufficient level of mechanically stability, i.e., to limit the frequency and size of the sudden, irreversible grain-rearrangement events that occasionally occur in compressed sphere packs [*Roux*, 2000]. A convenient way to achieve this condition is to subject loose sphere packs to several loading-unloading compression cycles up to stresses higher than the maximum intended for the numerical simulations (for details, see section 2.4).

2.2. Contact Force-Displacement Rule

One essential ingredient to include in DEM is a contact force-displacement rule. Because PS produces contacts that have a finite size when unloaded, we used *Digby*'s [1981] generalization of the Hertzian normal force-displacement rule (see *Elata and Berryman* [1996] or *Norris and Johnson* [1997] for discussions of contact force laws). A cross section of two unstressed, contacting spheres of radii r_i and r_j is shown in Figure 1a. The unstressed contact area has a radius a_0 and the distance between the centers at zero load is $h_0 = h_{i0} + h_{j0}$.

This configuration is equivalent to that of two identical spheres of radius r_{ij} with $2/r_{ij} = (1/r_i + 1/r_j)$. According to *Digby* [1981], a force, N_{ij}, normal to the contact plane will cause a converging motion of the centers of Δh_{ij}, where

$$N_{ij} = 2E\left[\frac{a_{ij}\Delta h_{ij}}{2} - \frac{\left({a_{ij}}^2 - a_0^2\right)^{\frac{3}{2}}}{3r_{ij}}\right] \tag{5}$$

with

$$2a_{ij}^2 = a_0^2 + \left(a_0^4 + r_{ij}^2\Delta h_{ij}^2\right)^{\frac{1}{2}}. \tag{6}$$

E is the Young's modulus of the solid and a_{ij} the radius of the stressed contact. Equations (5)–(6) reduce to the Hertzian force-displacement rule when a_0 is equal to zero. Note that if all length parameters are changed by a factor s, N_{ij} scales as s^2. This scaling relation implies that, for a given external isostatic pressure, p_c, the strains produced in identically structured sphere packs do not depend on grain size. The individual contact forces inside the sphere packs do, however, vary.

2.3. Approximate Pressure Solution Creep Rule for Individual Contacts

Our previous numerical methods (BE) cannot be implemented for a large number of mechanically coupled grain contacts. One solution is to seek an analytical expression describing the behavior of a single contact with a sufficient level of approximation and to incorporate it into DEM (see *Harthong et al.* [2009] for an example of this approach in the case of plastically compressed sphere packs). Fortunately, the following formula derived from LL provides a good approximation of the long-term convergence rates calculated in BE:

$$\frac{\mathrm{d}\Delta u_{ij}}{\mathrm{d}t} = \frac{2\frac{\Omega_s}{kT}\frac{N_{ij}}{\pi a_{ij}^2}}{\frac{2}{K_s} + \frac{\rho_s}{\rho_f}\frac{{a_{ij}}^2}{4Z}}, \tag{7}$$

where Δu_{ij} denotes the total thickness of the layers of dissolved solid on both sides of the contact interface, N_{ij} is here the effective normal force (i.e., accounting for the fluid pressure in the contact interface), and $Z = c_0\, w\, f_r\, D_m$ is the interface diffusivity coefficient. Dissolution at the grain contact affects the unstressed contact radius a_0 as depicted in Figure 1b (note that the elastic displacement Δh_{ij} and the stressed contact radius a_{ij} are not related through this geometry but obey equations (5)–(6), which take into account the elastic deformation of the spheres). Using the scaling properties of equations (5)–(6), it is clear that Δu_{ij} does not necessarily vary linearly with the scale factor s. The numerator of the right-hand side of equation (7) is scale independent, whereas the denominator is the sum of a scale-independent term and another one scaling as s^2.

In equation (7), we implicitly assume that the solute concentration in the pore space outside the contact interface is buffered at the equilibrium concentration c_0, perhaps owing to fast advective transport. Thus, precipitation on the free surface of the spheres is not included in the simulations. As a consequence, contact growth rates were likely minimized and strain rates maximized with respect to situations in which precipitation is active. Note also that equation (7) describes circular grain contacts, which do not intersect each other and, thus, applies only to configurations of relatively low density. Consequently, we stopped the simulations when the porosity of the compacted sphere packs reached 15%. In our experience, contact intersections are unlikely above this threshold.

2.4. Numerical Procedures

2.4.1. Preparing the Initial, Stress-Free Configuration

We constructed a set of 240 spheres with radii r_i assigned according to a uniform distribution (mean radius $r = 40$ μm, standard deviation $\sigma_r = 2.7$ μm). The spheres were placed into a cubic box with equal probability at all points in the box. The box was initially very large so that mutual interpenetration of the spheres did not occur. We then shrank the box isotropically, forcing the spheres to contact and to rearrange until the sides of the box (assumed perfectly rigid) supported pressures in excess of 120 MPa. After that, the box was reenlarged until the confining pressure returned nearly to zero. By repeating the entire loading-unloading cycle twice, we significantly reduced the number and magnitude of irreversible grain-rearrangement events, ensuring a sufficient level of mechanical stability. Lastly, we assigned the contact radii in the final (slightly stressed) configuration as the initial values of a_0 in equations (5)–(6) (Table 1), thus producing an exactly unstressed, yet rigid sphere pack. Here "rigidity" means that an infinitesimal contraction of the stress-free sphere pack will produce pervasive nonzero contact forces. Moreover, because new grain contacts form during compaction at unknown locations, we set an additional rule stating that the initial radius of any newly

Table 1. Dry Isostatic Compaction Characteristics: Confining Pressure p_c (MPa), Porosity ϕ, Total Number of Contacts n_c, Mean Coordination Number z_c, Mean Radius a_{grain} and a_{side} (μm) of Stressed Grain-Grain and Grain-Side Contacts, Respectively, Mean Contact Force N, and Standard Deviation σ_N (N)[a]

Characteristics	Values			
p_c	0	40	80	120
ϕ	0.434	0.409	0.395	0.383
n_c	716	838	880	904
z_c	5.2 (0.3)	6.2 (0.2)	6.6 (0.2)	6.8 (0.2)
a_{grain}	1.3 (0.3)	2.3 (0.3)	2.5 (0.4)	2.7 (0.4)
a_{side}	2.3 (0.8)	7.6 (2.2)	9.4 (2.6)	10.6 (3.0)
N	0	0.23	0.44	0.63
σ_N	0	0.18	0.34	0.48

[a]Uncertainties are given in parentheses.

formed grain contact was 0.2 μm. Ten spheres in the stress-free configuration (or 4% of the sphere population) were still loose, i.e., in contact with less than four other spheres. Loose spheres are very hard to eliminate completely in numerical simulations and do, in fact, exist in real, unconsolidated, granular materials. Elastic wave data show that natural sands contain on the order of a few percent of loose grains, called "rattlers" because of their response to impinging elastic waves (J. D. Berryman, personal communication, 2012).

2.4.2. Dry Isostatic Compaction

In order to simulate dry isostatic compaction, we started from the stress-free configuration described above and isotropically shrank the box by 0.02 μm increments, letting the spheres rearrange until the contact forces balanced to within 10^{-6} N. At each of these steps, we computed the pressures $p_x = N_x\, l^{-2}$, $p_y = N_y\, l^{-2}$, and $p_z = N_z\, l^{-2}$, where N_x, N_y, and N_z are the magnitudes of the total contact forces acting on the sides, and l is the current length of the box. We observed that p_x, p_y, and p_z constantly approached the mean pressure $p_c = (p_x + p_y + p_z)/3$ (hereafter called confining pressure) within 4% or less, thus confirming that the simulated compaction process was nearly isostatic.

2.4.3. Isostatic PS Creep

To simulate isostatic PS creep, we selected conditions of temperature (i.e., 773, 873, or 973°K) and confining pressure (i.e., 40, 80, or 120 MPa) and set the initial sphere configuration to be the one produced during dry compaction at the assigned value of p_c, where p_c now denotes the effective pressure (i.e., taking the fluid pressure into account). These values are consistent with those chosen for many experiments, but not necessarily for conditions under which natural deformation by pressure solution is thought to occur. The ultimate goal, of course, is to develop a constitutive law, which may be scaled over a broad range of conditions. From equation (7), we calculated the thickness Δu_{ij} of the solid layer dissolved at each grain-grain and grain-side contact during a time increment Δt. The box sides were assumed insoluble. We continued by updating the unstressed contact radii a_0 for each contact using the values of Δu_{ij} and then calculating the corresponding drop in confining pressure experienced by the relaxed sphere pack. Finally, we shrank the box isotropically by an amount determined by trial and error until the original value of p_c was restored. We did not need to consider individual values of p_x, p_y, and p_z separately, because they always remained nearly equal. The sequence of computations described above was repeated as many times as desired, yielding the total linear deformation of the sphere pack (i.e., $\varepsilon_x = \varepsilon_y = \varepsilon_z$) as a function of time. We emphasize that the displacements of the box sides correspond to the cumulated effect of all the individual dissolution and "elastic" displacements, Δu_{ij} and Δh_{ij}. In consequence, ε_x can be viewed as the sum $\varepsilon_{dis} + \varepsilon_{el}$ of a dissolution and an elastic strain term, although ε_{dis} and ε_{el} cannot be separated in practice.

In order to save CPU time we progressively increased Δt from about 1000s at early simulated times to 10^9s at late times (corresponding to maximum Δu_{ij} values at individual contacts of 0.0001 to 0.05 μm, respectively). Relevant geometrical, topological, and mechanical parameters including porosity, contact radius, coordination number, and contact force distribution were monitored during both dry compaction and PS creep simulations. We restricted this study to simulated deformation of quartz aggregates, using the following temperature-dependent values of K_s, c_0, and D_m (see references in LL and BE):

$$K_s = 2.27 \times 10^{-(3.826 + 0.002028T + 4158/T)} \quad (\text{in m s}^{-1}),$$

$$c_0 = 0.055 \times 10^{-(0.254 + 1107.12/T)},$$

$$D_m = 9 \times 10^{-7} \exp(-15000/8.31036T) \quad (\text{in m}^2\ \text{s}^{-1}).$$

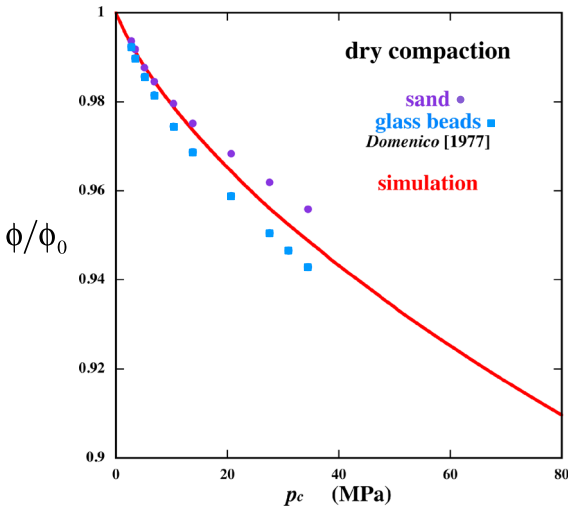

Figure 2. Plot of the reduction in normalized porosity ϕ/ϕ_0 with increasing confining pressure p_c (red line). The simulated curve agrees well with *Domenico*'s [1977] experimental data on compacted dry sand (purple dots) and glass beads (blue squares).

The interface thickness w was assumed equal to 10^{-8} m, and we simulated conditions of fast and slow diffusion by considering two values of the diffusion retardation factor f_r, namely 1 and 10^{-3}, corresponding to the interface diffusivity coefficient Z on the order of 10^{-18} and 10^{-21} m^3 s^{-1}, respectively.

The scaling properties of equations (5)–(6) provide a simple way to investigate the effect of grain size on PS creep. Indeed, any of the sphere configurations generated during the dry isostatic compaction stage can be geometrically scaled by an arbitrary factor s without changing the confining pressure externally applied to it. PS creep of the scaled sphere packs can then be simulated with the procedures described above using properly scaled parameters. Note, however, that we kept the diffusivity coefficient Z constant and thus did not scale the interface thickness w.

2.4.4. One-Dimensional Simulations

We performed additional, one-dimensional (1-D) PS creep simulations, in which the number of contacts did not change. Specifically, we placed 10 identical spheres of radius 40 μm with contacts lying on a straight line (the x direction). The end spheres were in contact with two side planes perpendicular to x. The relative positions of the spheres were such that the initial values of a_0 were equal to the averages of those obtained in the three-dimensional (3-D) simulations for the grain-grain and grain-side contact (Table 1). We then applied the same numerical methods as before, except that only displacements in the x direction were allowed. Complete immersion of the spheres in the solvent fluid was, of course, assumed but, because free surface precipitation was excluded, the amount of fluid surrounding the spheres did not have to be specified. Equal and opposite contact forces were applied to the end spheres in two different ways: (a) constant side forces, $N_x = 4r^2 p_x$, simulating oedometric compression (i.e., uniaxial compression with no lateral deformation, $\varepsilon_y = \varepsilon_z = 0$), where p_x denotes the effective axial stress, and (b) side forces decreasing with increasing linear deformation, $N_x = 4r^2(1 - \varepsilon_x^2)p_c$, corresponding to changes in lateral dimensions consistent with $\varepsilon_x = \varepsilon_y = \varepsilon_z$ and, therefore, simulating isostatic compression with unchanging packing geometry.

3. Results

3.1. Dry Compaction

Simulating dry compaction simulation was not our main focus and a detailed discussion of that process is beyond the scope of this paper. But, describing the geometry of packing and the stresses within the aggregate was an obligatory initial step, necessary for subsequent simulation of PS creep. To test the simulations against experiments, we compared the simulated porosity reduction with increasing confining pressure to that of compacted dry sand and glass bead packs [*Domenico*, 1977; *Makse et al.*, 2004]. Although the calculated sphere pack had an unstressed porosity ϕ_0 of 0.434, which was larger than the experimental packs, the curves of normalized porosity ϕ/ϕ_0 versus p_c compare well (Figure 2). The geometry and topology of the simulated grain contact network changed significantly during dry compaction, even though the decrease in porosity was only a few percent. The total number of contacts n_c and the mean coordination number z_c grew by about a third when p_c increased from 0 to 120 MPa (Table 1). The mean radius of the grain-grain contacts, a_{grain}, was significantly lower than that for grain-side contacts, a_{side}, and the difference between the two progressively increased with stress: a_{grain} and a_{side} grew by factors of about 2 and 5, respectively. As expected, increasing p_c produced a linear increase of the mean contact force, N. There was no diminution, however, of the heterogeneity in contact forces, as evidenced by an increasing standard deviation, σ_N (Table 1).

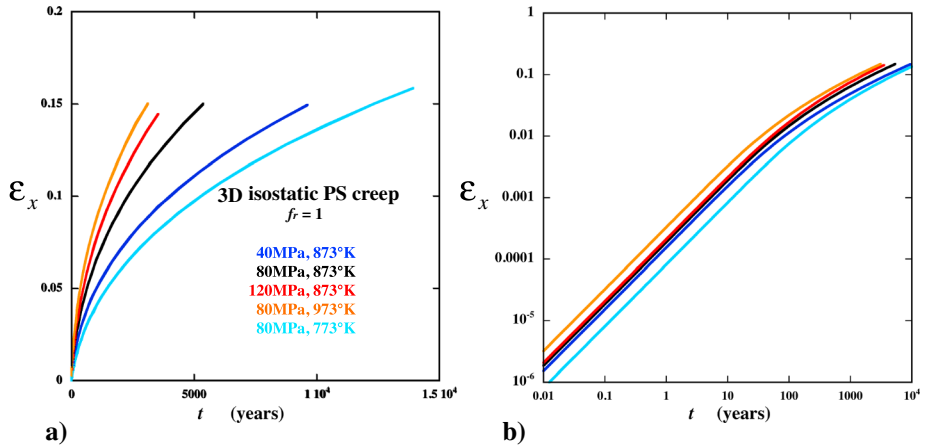

Figure 3. Plots of strain, $\varepsilon_x = \varepsilon_y = \varepsilon_z$, versus time for five simulated 3-D isostatic compressions of the sphere pack in fast diffusion conditions ($f_r = 1$). The color of each curve corresponds to the values of temperature and confining pressure indicated in the inset. The curves are represented in (a) linear and (b) log-log scales.

3.2. Pressure Solution Creep

Figure 3 shows the calculated (isostatic) strain in the sphere pack, $\varepsilon_x = \varepsilon_y = \varepsilon_z$, as a function of time for five combinations of temperatures and confining pressures when interface diffusion was fast (i.e., $f_r = 1$). In all cases, the creep curves were nonlinear and regularly decelerated with time. Strain rates generally increased with increasing T or p_c (Figure 3a). One-dimensional simulations yielded curves with roughly similar shape, but slightly faster strain rates than those in 3-D (Figure 4a). When the simulated data are plotted in log-log scale (Figure 3b), two successive power law ($\varepsilon_x \propto t^{\xi}$) regimes are evident: at early simulated times, i.e., $t < 10$ to 20 years, ε_x varied linearly with t ($\xi = 1$), but at later times, creep rates decreased, and a second power law dependence with $\xi < 1$ emerged at $t > 100$ to 200 years. These power laws, although not exact, can be used as approximate descriptions for behavior at early and late times. The 1-D simulations also presented similar early and late power law regimes, indicating that this behavior was not caused by changes in packing but resulted from the LL kinetics at individual contacts (equation (7)). Noting that $\varepsilon_x \propto t^{\xi}$ implies $d\varepsilon_x/dt \propto t^{-\alpha}$ and $d\varepsilon_x/dt \propto \varepsilon_x^{-\beta}$, with $\alpha = 1 - \xi$ and $\beta = (1 - \xi)/\xi$, we can assess the accuracy of the approximate power law description by checking the relationships of the exponents α and β to ξ at a given time. The early-time linear regime was remarkably well delineated in all cases. For the late-time regimes, the exponents ξ, α, and β satisfactorily verified the mutual relationships mentioned above for

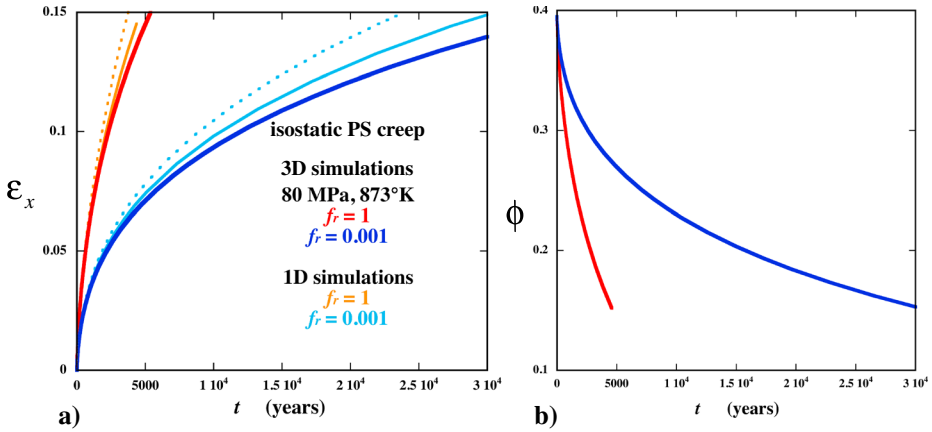

Figure 4. Examples of curves of simulated (a) strain and (b) porosity versus time for fast and slow interface diffusion ($f_r = 1$, red and orange lines, $f_r = 0.001$, blue lines) and for 3-D isostatic (red and dark blue lines), 1-D isostatic (solid orange and light blue lines), and 1-D oedometric compressions (dotted orange and light blue lines). These simulations were performed using a temperature of 873°K and an effective pressure of 80 MPa.

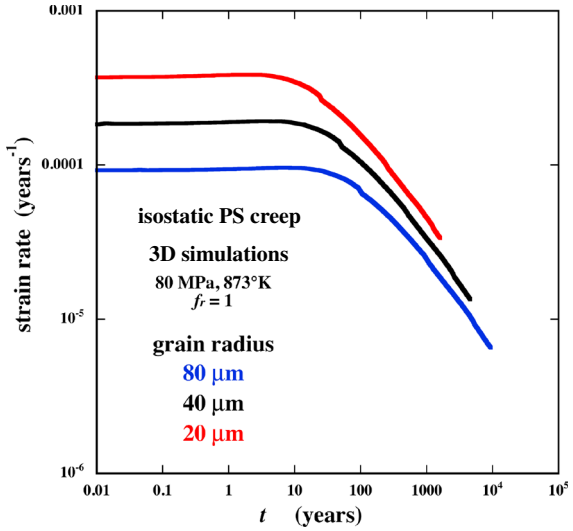

Figure 5. Examples of curves of simulated strain rate versus time for identically structured sphere packs, scaled to three values of the mean grain radius (blue, 80 μm, black, 40 μm, and red, 20 μm). These 3-D simulations were performed using a temperature of 873°K, an effective pressure of 80 MPa and a diffusion retardation factor $f_r = 1$.

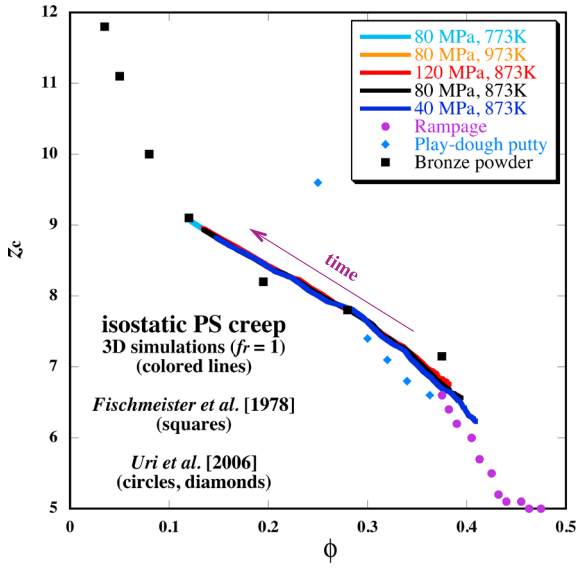

Figure 6. Examples of curves of the mean contact coordination number z_c versus porosity. These 3-D simulations were performed using a diffusion retardation factor $f_r = 1$ and values of temperature and effective pressure indicated in the inset. By and large, the five curves are tightly superposed, suggesting the existence of a single, general relationship between z_c and ϕ. For comparison, we plotted values of the mean contact coordination number experimentally measured in plastically deformed aggregates (black squares, bronze powder [*Fischmeister et al.*, 1978]; blue diamonds, play-dough putty spheres [*Uri et al.*, 2006]). The results of *Rampage* numerical simulations [*Uri et al.*, 2006] are also represented (purple dots).

the 1-D oedometric simulations, while a somewhat poorer accord was observed for the 1-D and 3-D isostatic simulations. Although variations occurred, ξ measured at later times was rather weakly dependent on temperature and pressure as demonstrated by the parallelism of the $\varepsilon_x(t)$ creep curves in Figure 3b. Simulations performed for fast and slow interface diffusion (i.e., $f_r = 1$ and 0.001, respectively) yielded similar $\varepsilon_x(t)$ and $\phi(t)$ creep curves, albeit stretched over different intervals of time (Figure 4). PS creep rates decreased significantly with increasing grain size and the transition from early- to late-time regimes was delayed, but there was no visible change in the exponent α (Figure 5).

Significant changes in grain packing occurred during the simulations. In particular, the mean coordination number z_c increased strongly with increasing time and decreasing porosity (Figure 6). The relationship between z_c and ϕ (Figure 6) seems to be quite general. It was essentially independent of pressure and temperature and, more generally, held in conditions of both fast and slow interface diffusion and for other realizations of sphere packs with slightly different initial porosity and contact radius distribution. The packing changes were accompanied by a 50% reduction of the mean contact force N (Figure 7a), nearly twice as much as the 30% drop in externally applied force needed to maintain a constant p_c on a 15% isostatically compacted sphere pack. We also observed a considerable decrease of the standard deviation of the contact forces σ_N (Figure 7b), implying an increasingly uniform distribution of contact forces. The increased uniformity of contact force was not, however, accompanied by a similar homogenization of the contact sizes. In fact, the grain-side contacts grew more during PS creep than their grain-grain counterparts, thus increasing the contrast between the two contact families.

4. Discussion

4.1. Comparison of Simulations With Previous Constitutive Relations

Early constitutive models of pressure solution [e.g., *Weyl*, 1959; *Elliot*, 1973; *Paterson*, 1973; *Rutter*, 1976; *Raj*, 1982; *Gratz*, 1991] were constructed in a form inspired by the classic grain boundary diffusion (or Coble) creep model. Later extensions considered the effect

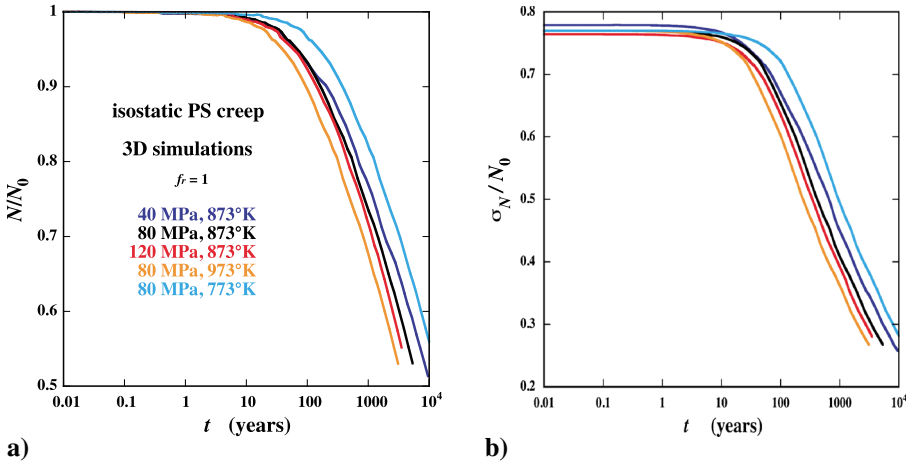

Figure 7. Examples of curves of (a) the mean contact force N and (b) the standard deviation of the contact forces σ_N normalized to the initial mean contact force N_0. These 3-D simulations were performed using a diffusion retardation factor $f_r = 1$ and values of temperature and effective pressure indicated in the inset.

of dissolution at the contact interface on the creep kinetics [e.g., *Schutjens*, 1991; *Paterson*, 1995]. When a single mechanism is rate limiting, the constitutive laws often take the form:

$$\frac{d\varepsilon_x}{dt} = G\frac{\Omega_s}{kT}\exp\left(\frac{-H}{RT}\right)\frac{{p_c}^n}{d^m}, \tag{8}$$

where G is a constant, H the effective PS activation enthalpy, R the gas constant ($R = k/N_A$, where N_A is Avogadro's number), $d = 2r$ the grain size, n the stress exponent (usually assumed equal to one), and $m = 1$ or 3 depending on whether the rate-limiting step is dissolution or diffusion, respectively. However, strain rates in aggregate compaction experiments are normally observed to decrease with decreasing porosity and cannot be described by equation (8). Thus, modifications have been proposed to account for changes of packing geometry and contact area, the most common being the inclusion of a separable exponential factor containing porosity [e.g., *Rutter and Wanten*, 2000; *Niemeijer et al.*, 2002; *Fitzenz et al.*, 2007]:

$$\frac{d\varepsilon_x}{dt} = G\frac{\Omega_s}{kT}\exp\left(\frac{-H}{RT}\right)\frac{{p_c}^n}{d^m}\exp(q\phi), \tag{9}$$

where q is an empirically determined constant and porosity ϕ is a decreasing function of time. When pressure, temperature, and grain size are fixed, equation (9) predicts linear dependence of $\log(d\varepsilon_x/dt)$ on ϕ. In addition, because the principal strain rate is $-1/3$ the volumetric strain rate, the porosity at time t is the following [*Fitzenz et al.*, 2007, equation (2)]:

$$\phi = \frac{-1}{q}\log[Kqt + \exp(-q\phi_0)] \tag{10}$$

and

$$3\frac{d\varepsilon_x}{dt} = \frac{K}{Kqt + \exp(-q\phi_0)}, \tag{11}$$

where ϕ_0 is the starting porosity and $K = 3G\frac{\Omega_s}{kT}\exp\left(\frac{-H}{RT}\right)\frac{{p_c}^n}{d^m}$. However, the simulated data did not show linear relationships of $\log(d\varepsilon_x/dt)$ with porosity nor of the inverse strain rate with time (Figures 8b–8c). Therefore, the simulations do not support equation (9). Instead, two successive power law regimes, $d\varepsilon_x/dt \propto t^{-\alpha}$, can be identified (Figures 5 and 8a). The first is at early times, where $d\varepsilon_x/dt \propto t^0$; and the second at late times, where α is approximately 0.6–0.7 and creep rates decelerate. The late-time exponent ξ relating strain to time (or its counterparts α and β) had a moderate range of variation from one simulation geometry to another, the lowest values ($\xi \approx 0.3$) being obtained for the 3-D simulations and the largest ($\xi \approx 0.6$) for the 1-D oedometric ones (Table 2).

4.2. Apparent Stress Exponent, Activation Enthalpy, and Grain-Size Exponent

Workers often apply the aggregate creep law (equation (9)) to experimental data to calculate apparent values of the stress exponent, activation enthalpy, and grain-size exponent. The empirical values obtained are then

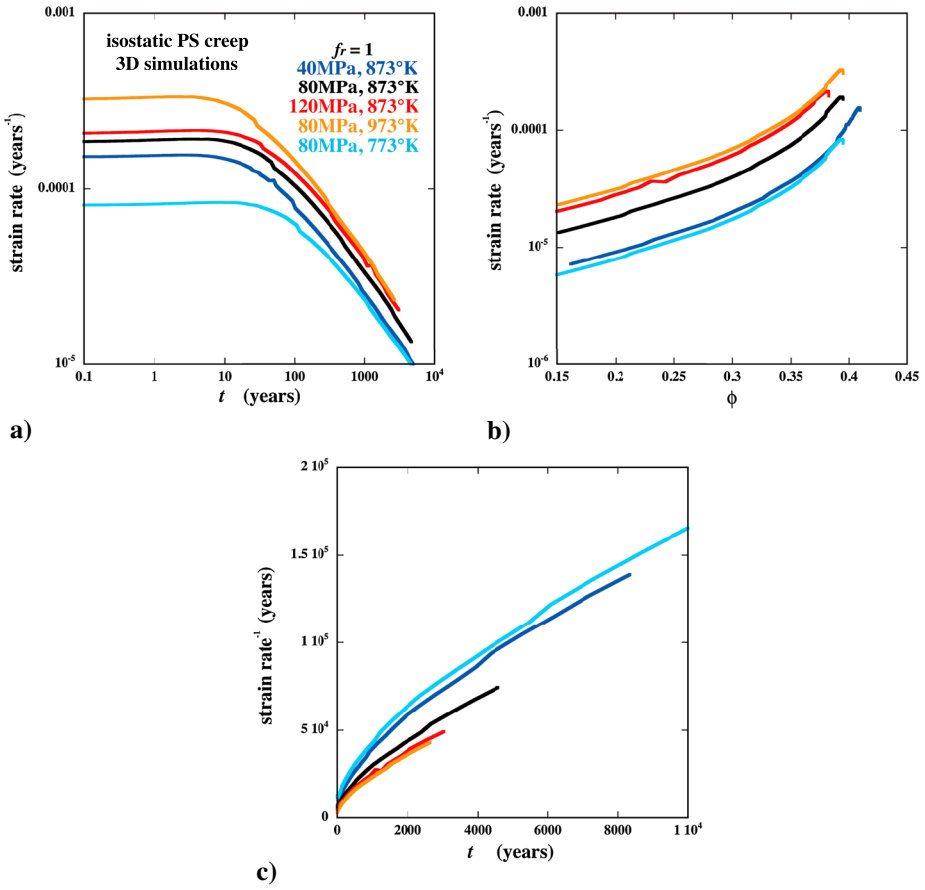

Figure 8. Examples of curves of (a) strain rate versus time, (b) strain rate versus porosity, and (c) inverse strain rate versus time demonstrating that the simulations based on LL kinetics were not well described by the generic aggregate constitutive laws expressed in equation (9) but instead obeyed the empirical, double power law constitutive behavior discussed in the text. These 3-D simulations were performed using a diffusion retardation factor $f_r = 1$ and values of temperature and effective pressure indicated in the inset.

compared to those independently identified with diffusion or dissolution kinetics. Here we use the simulations as experimental data to be analyzed using the aggregate flow law. Following *Visser et al.*'s [2012, Figures 6–7] graphic approach, we plotted the simulated strain rates (measured at constant strain levels) versus p_c, $1/T$, or r and interpreted them in terms of apparent values of n, H, and m (Figures 9 and 10). The results can be summarized as follows:

1. Stress exponent
   In all simulations, the effective stress exponents increased with increasing strain (or time) assuming values about 0.3 at strains less than 1%, to about 1 for strains approaching 15% (Figure 9a). The stress exponents

Table 2. Summary of the Constitutive Parameters for the Various 3-D and 1-D Simulations: The Late-Time Exponent ξ, the Early- and Late-Time Activation Enthalpies H_0 and H_∞ (kJ mol^{-1}), and the Stress Exponents n_0 and n_∞[a]

	Three-Dimensional		One-Dimensional			
			Isostatic		Oedometric	
f_r	1	0.001	1	0.001	1	0.001
ξ	0.43 (0.05)	0.34 (0.03)	0.50 (0.03)	0.41 (0.04)	0.56 (0.01)	0.41 (0.01)
H_0	43	42	43	42	43	42
n_0	0.28	0.28	0.33	0.32	0.34	0.34
H_∞	19	11	22	13	24	13
n_∞	0.39	0.29	0.48	0.38	0.50	0.38

[a]Uncertainties are given in parentheses.

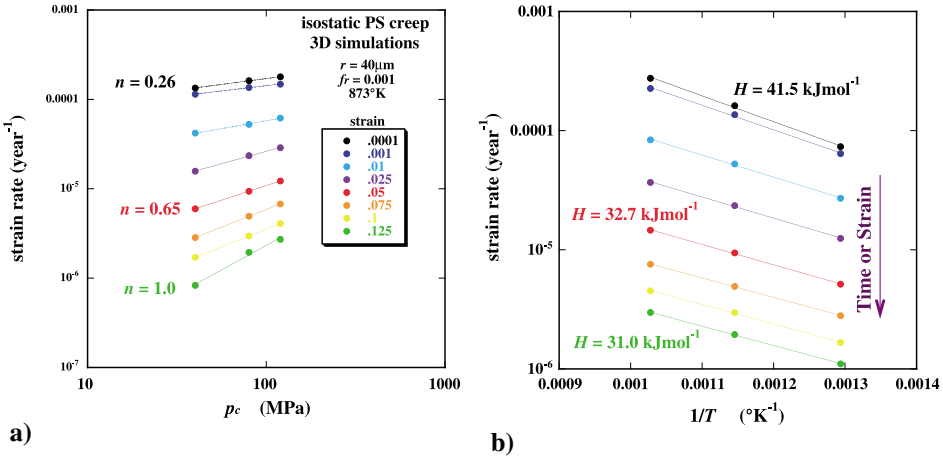

Figure 9. Examples of plots of simulated strain rates (measured at constant strain levels as indicated by the various colors and values given in the inset) versus (a) effective pressure p_c and (b) inverse temperature $1/T$. From these diagrams, we calculated the apparent values of the stress exponent n and activation enthalpy H (a few values are indicated near the data points in corresponding colors). The particular 3-D simulations included here were performed in conditions of slow interface diffusion ($f_r = 0.001$).

were slightly greater in fast diffusion conditions and in 1-D simulations (Figure 10). These generally low stress exponents differ from the classic aggregate models, which predict $n = 1$ [e.g., *Rutter*, 1976; *Paterson*, 1995], and from those found in many experimental studies, which often are much larger than unity. For example, *Niemeijer et al.* [2002] found stress exponents of 3 to 3.6 during compaction of quartz sand packs at temperatures of 400–600°C and lithostatic effective pressures of 50–150 MPa (a slightly lower value of 2.5 was obtained by *Fitzenz et al.* [2007], who used a more accurate Bayesian inference method to reinterpret Niemeijer et al.'s data).In contrast, low apparent stress exponents were observed in experiments by *Visser et al.* [2012], who compacted sodium nitrate sphere packs at low loads. The conditions in these tests were almost identical to that assumed in the simulations. The grains were nearly spherical in shape. Because effective stresses were lower than 5 MPa, fracture and grain cracking were suppressed even during cold pressing, and because the dissolution and diffusion kinetics of the highly soluble nitrate were very rapid, other strain mechanisms were likely absent. In order to determine apparent values of n, we used data from Visser et al.'s Figure 6, excluding data corresponding to stresses lower than 0.016 MPa. According to the authors, strain rates in those conditions may have been influenced by smoothing owing to surface tension, an effect omitted in the simulations. The apparent stress exponents in the nitrate experiments increased from 0.24 at low strains to values between 1 and 2 at large strains. The simulations agree most closely with experiments where grain sizes were near $2r = 80$ μm, as in the simulations. The highest and most incompatible values of n occurred for the finer-grained materials (see Figure 10, where the experimental data were translated to the left to aid the comparison to the numerical results).

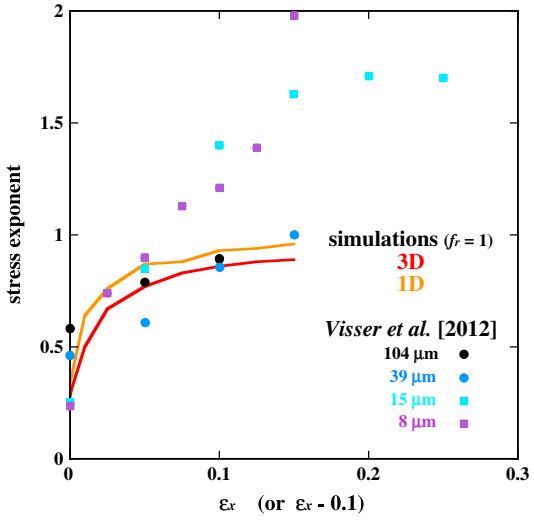

Figure 10. Comparison of simulated (red and orange lines) and experimentally measured (black, blue, and purple symbols) values of the apparent stress exponent n for various strain levels. The particular simulations included here were performed using a diffusion retardation factor $f_r = 1$ and a temperature of 873°K. The experimental data were obtained from *Visser et al.*'s [2012] Figure 6. The values of the experimental stress exponent were translated to the left to help comparison with the simulated values.

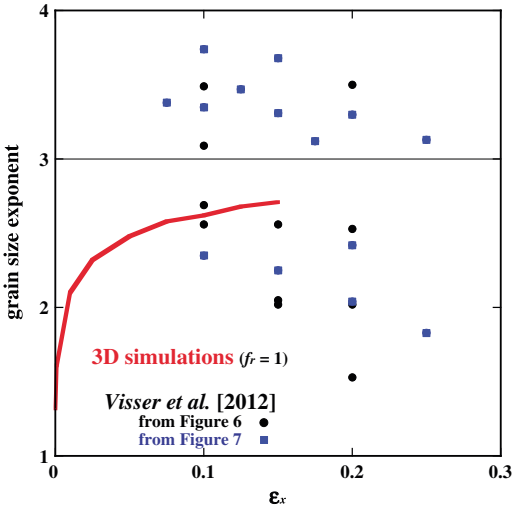

Figure 11. Comparison of simulated (red line) and experimentally measured (black and blue dots) values of the apparent grain-size exponent m for various strain levels. The particular 3-D simulations included here were performed using a diffusion retardation factor $f_r = 1$, an effective pressure of 80 MPa and a temperature of 873°K. The experimental data were obtained from *Visser et al.*'s [2012] Figures 6 and 7. The experimental grain size exponents had an average of 2.8 and a standard deviation of 0.6.

2. Activation enthalpy
   Values for the apparent activation enthalpy H were essentially the same in 1-D and 3-D simulations with equivalent process kinetics. But, in all cases, H was strongly affected by the interface diffusion coefficient. When diffusion was slow (i.e., $f_r = 0.001$), H regularly decreased with increasing strain (or time) from 41.5 to 31 kJ mol^{-1}. The rate of transition from high to low values was also affected by f_r: H remained essentially constant near 43.3 kJ mol^{-1} in fast diffusion conditions ($f_r = 1$), while additional 1-D simulations using the extremely low value $f_r = 10^{-5}$ showed that H reached a minimum value of about 29 kJ mol^{-1} within less than 0.1% strain and stayed constant afterward. A similar decrease of the apparent activation enthalpy with time was also inferred from the single asperity simulations of BE, who attributed it to contact growth with time. Overall, the apparent values of H tended to be lower than expected. At early times, when dissolution was most likely to be dominant, H was significantly lower than the dissolution activation enthalpy $H_{dis} \approx 72$ kJ mol^{-1}. At late times, when diffusion kinetics are probably most important, we measured H's slightly lower than the effective activation enthalpy $H_Z \approx 36$ kJ mol^{-1} of the interface diffusivity coefficient Z. These results (especially for early times) may be partially explained by the fact that only the total strain rate $d\varepsilon_x/dt = d\varepsilon_{dis}/dt + d\varepsilon_{el}/dt$ (not $d\varepsilon_{dis}/dt$ alone) are retrieved in the analysis [see *Bernabé et al.*, 2009].
3. Grain-size exponent
   As was true for activation enthalpy, the grain-size exponent, m, determined from the simulations, was primarily controlled by the diffusion retardation factor f_r. For fast diffusion ($f_r = 1$), we found $m \approx 1$ independent of time (or strain) whereas, when diffusion was slow ($f_r = 0.001$), m progressively increased from 1.3 to about 3 with increasing strain (Figure 11). Unlike the stress systematics, the influence of grain size is in general accord with the aggregate constitutive law. For comparison with experiments, we examined the curves of strain rate versus grain diameter presented in *Visser et al.*'s [2012] Figure 7. In the finest-grained materials, the experimental strain rates increased with d, reaching a maximum near $d \approx 20$ μm, and then monotonically decreased as predicted by the classic models. The authors attribute the positively inclined portions of the $d\varepsilon_x/dt$ versus d curves to the surface tension effect mentioned earlier, leading to deceleration of creep (and possibly arrest as required by the viscoplastic model of *Revil* [1999, 2001]). Accordingly, we thus estimated m from the strain rate data of Figure 7 corresponding to $d > 20$ μm. Since the data sets represented in Visser et al.'s Figures 6 and 7 are not identical, we also determined m from cross plotting the data of Figure 6 for all grain sizes, including 8 and 15 μm. Values of m varying from 1.5 to 4.1 (with an average of 2.8 and a standard deviation of 0.6) were obtained.

4.3. Evolution of the Sphere Pack Structure

The simulations revealed a relationship between the mean contact coordination number, z_c, and porosity, ϕ, that was generally valid, except perhaps at the highest porosities (Figure 6). This relationship agreed well with data collected during plastic compaction of packs of bronze powder [*Fischmeister et al.*, 1978] and play-dough spheres [*Uri et al.*, 2006] (Figure 6). *Uri et al.* [2006] also numerically simulated sphere packs elastically compressed by gravity. Their results for sphere packs with porosities near 0.4 were similar to that in our calculations of dry compaction. Hence, this general insensitivity to differences in deformation mechanisms suggests that the ϕ-z_c relationship of Figure 6 may be characteristic of a broad class of partially consolidated porous media.

As shown in Figure 7a, the mean contact forces decrease quickly as the material compacts. There are two transient effects that might be responsible: one is the increase in coordination number with decreasing

porosity, the second is the transient associated with changing kinetics at the grain contacts [BE]. The relative importance of the two transients can be gauged by comparing the results of the 3-D and 1-D simulations (Figure 4a); only the former simulations have changes in packing. We note that creep rates were slowest for 3-D isostatic compaction and fastest for 1-D oedometric compaction. In fast diffusion conditions (i.e., $f_r = 1$), strains = 14% were reached in 4640, 4070, and 3330 years in the 3-D isostatic, 1-D isostatic, and 1-D oedometric simulations, respectively; 30,200, 25,400, and 20,200 years were necessary for the same geometries when diffusion was slow (i.e., $f_r = 0.001$). In the 1-D oedometric simulations, the strain rate deceleration was exclusively caused by the decline in contact stress associated with growth of the contact. An additional strain rate deceleration of about 15 to 20% occurred in the 1-D isostatic simulations owing to the decrease in externally applied contact force. Finally, in the 3-D simulations, additional changes in the packing geometry produced a further deceleration of around 10 to 15%. The relatively small deceleration caused by changes in z_c can be attributed to the low sensitivity of creep rate to the contact load, as evidenced by the low apparent stress exponents discussed above. If the stress exponents were higher (as often observed in aggregate compaction experiments), the relative deceleration caused by packing changes will likely be much greater.

4.4. Empirical Power Law Dependence of Strain Rate and Strain on Time

Because there is no analytical formulation of the aggregate behavior that incorporates the LL kinetics at the grain contacts, we sought an empirical description. As noted above and shown in Figures 3, 5, and 8, the creep behavior can be approximated by an empirical double power law relation between time and either strain or strain rate. Power laws of the form $\varepsilon_x \propto t^{\xi}$ with $\xi \cong 0.3$–0.4 have actually been observed at late times in the experiments of *Renard et al.* [2001] (oedometric compaction of salt/clay mixtures; $\xi = 0.4$) and *Dysthe et al.* [2003] (single cylindrical indenter; $\xi = 1/3$). Most interesting is the agreement with *Visser et al.*'s [2012] experiments because the aggregate geometry most closely resembles the present numerical simulations. Visser et al.'s results, when plotted as curves of strain rate versus strain (volumetric strain and axial strain are equal in oedometric systems), visibly displayed two successive power laws $d\varepsilon_x/dt \propto \varepsilon_x^{-\beta}$ (see Visser et al.'s Figure 5b). Although experimental and simulation results agree very well qualitatively, there are large quantitative differences in rates, possibly due to the different minerals used (e.g., $NaNO_3$ is much more soluble and deformable than quartz). In particular, the transition between the early- and late-time regimes occurred at a much greater strains in Visser et al.'s experiments than in the simulations ($\varepsilon_x \approx 10\%$ instead of 0.1%) and the exponent β took much greater values ($\beta \approx 1$ at early times instead of 0 and $\beta \approx 10$ at late times instead of between 1 and 2).

4.5. Interpretation of Aggregate Compaction Based on the LL Kinetics

Because the double power law behavior observed in both the 1-D and 3-D simulations was similar, we infer that the changes in packing geometry and distribution of contact forces are not dominantly responsible for the relation between time and strain. Thus, the apparent values of n, H, and m measured in the aggregate are most likely influenced by transients associated with the LL kinetics (equation (7)). It is therefore interesting to examine the properties of equation (7) in detail.

1. Stress exponent
   At early times, the initial contact radius a_0 was very small. By plugging $a_0 \approx 0$ in equations (5)–(6), we find that the stressed contact radius a_{ij} is proportional to ${N_{ij}}^{1/3}$. Since we can estimate the effective pressure applied on a single contact as $p_c \approx N_{ij}/4{r_{ij}}^2$, equation (7) can be rewritten in the following form:

$$d\varepsilon_{dis}/dt \propto du_{ij}/dt = \frac{\lambda_1 \frac{p_c}{p_c^{2/3}}}{\lambda_2 + \lambda_3 p_c^{2/3}} \tag{12}$$

   where λ_1, λ_2, and λ_3 are positive parameters insensitive to the applied contact pressure. Equation (12) implies that $-1/3 \le n \le 1/3$. An apparent stress exponent $n \approx 1/3$ should be expected when PS is dissolution controlled (i.e., $\lambda_2 >> \lambda_3 {p_c}^{2/3}$) whereas diffusion-controlled should be indicated by much lower (possibly negative) values of n. At late times, owing to contact growth (i.e., large a_0), $a_{ij} \approx a_0$ becomes independent of p_c and the ${p_c}^{2/3}$ actors in equation (12) disappear, i.e., $d\varepsilon_{dis}/dt \propto \lambda_1 p_c/(\lambda_2 + \lambda_3)$, implying that n approaches unity. Thus, equation (7) explains the observed increase of n from about 1/3 at very low strains to 1 at large strains (Figure 10). We note that *Visser et al.*'s [2012] experiments display a similar behavior, except that the strains are much larger in general and stress exponents between 1 and 2 occurred at large strains for the fine-grain materials.

Extra processes not included in the simulations are required to explain $2 \le n \le 1$. One possibility is a pressure dependence of the effective interface thickness w, which would yield $d\varepsilon_{dis}/dt \propto \lambda_1 p_c/(\lambda_2 + \lambda_3/p_c)$ in the large strain limit (i.e., at late times) and $n \approx 2$ when λ_3 dominates λ_2 (in other words, when PS is diffusion controlled).

2. Activation enthalpy
   The combined temperature dependence of the parameters in equation (7) can rewritten as follows:

$$d\varepsilon_{dis}/dt \propto \frac{\frac{\kappa_1}{T}}{\frac{\kappa_2}{\exp(-H_{dis}/RT)} + \frac{\kappa_3}{\exp(-H_Z/RT)}} \tag{13}$$

   where κ_1, κ_2, and κ_3 are quantities that do not depend on temperature. The creep rate in this model, clearly, does not obey a simple Arrhenius relation, and thus, the apparent activation enthalpy, H_{app} may take somewhat unexpected values. However, H_{app} should approach H_{dis} or H_Z, if one of term in the denominator is negligible with respect to the other. Because κ_3 contains a_{ij}, its magnitude increases with time while κ_2 remains constant. Then H_{app} should evolve toward H_Z with increasing time, as is, in fact, observed in the slow diffusion simulations. This trend should also apply to fast diffusion simulations, but we did not observe it, perhaps because of limits in the duration of the simulations.

3. Grain-size exponent
   Owing to the scaling properties previously discussed in section 2.3, equation (7) can be recast as follows:

$$d\varepsilon_{dis}/dt \propto \frac{1}{s} du_{ij}/dt = \frac{\gamma_1}{\gamma_2 s + \gamma_3 s^3} \tag{14}$$

   where γ_1, γ_2, and γ_3 are parameters independent of grain scale. Since it is equivalent to express the scale dependence of $d\varepsilon_{dis}/dt$ in terms of the scaling factor s or the grain size $2r$, equation (14) recovers a feature of the classic PS models, namely, that the grain-size exponent m should lie between 1 and 3, with the bounds 1 and 3 corresponding to dissolution- and diffusion-controlled PS creep, respectively. As in the previous paragraph, γ_3 increases with time while γ_2 remains constant. As a consequence, m must vary with time from 1 to 3, as was observed in the slow diffusion simulations. The values of m determined from *Visser et al.*'s [2012] data tend to cluster near 3 and, therefore, indicate a dominant effect of interface diffusion, a reasonable conclusion given the high solubility of $NaNO_3$.

5. Conclusion

The simulations reported here used a constitutive model formulated by LL to describe pressure solution along grain/grain contacts. The LL model is founded on a local definition of the thermodynamic driving force and leads to a fully coupled formulation of elastic deformation, dissolution, and diffusive transport along the grain boundaries. Thus, we can use the simulations to assess the effects on the aggregate compaction rates when diffusion and dissolution are fully coupled at the microscopic scale and when packing geometry changes substantially.

Our main result is that the simulated strain rates were not well described by the generic aggregate constitutive laws expressed in equation (9). Instead, we observed the following that:

1. The simulated strain data could be empirically fitted by two successive power laws of the form, $\varepsilon_x \propto t^{\xi}$, where ξ was equal to 1 at very early times, but dropped to as low as 0.3 at longer times;
2. The apparent sensitivity of strain rate to stress found in the simulations was very low (apparent stress exponent significantly lower than 1);
3. The apparent activation enthalpy obtained from the simulated data was intermediate between that assumed for dissolution and diffusion and further tended to decrease with time;
4. The influence of grain size on strain rates was in general accord with the generic aggregate constitutive law, although the apparent grain-size exponent was time dependent in some conditions.
5. We observed large changes in packing during the simulations.

These characteristics are a consequence of the LL kinetics embodied in equation (7). Remarkably, similar features can also be observed in the experiments of *Visser et al.* [2012], the only ones to our knowledge, which were run using an aggregate geometry and physical conditions closely resembling the present numerical simulations. The increase in coordination number with decreasing porosity agreed well with the experimental results of

Fischmeister et al. [1978] and *Uri et al.* [2006] on plastically deformed aggregates. The variations in packing, however, had a limited effect on the simulated strain rates. This weak sensitivity of strain rates to packing was caused by the weak sensitivity to stress associated with equation (7). Much greater effects may be expected in situations when additional, strongly stress-dependent mechanisms are involved at the grain contacts.

Acknowledgment
This project was supported by the U.S. Department of Energy under grant DE-FG09-97ER14760.

References

Agnolin, I., and J.-N. Roux (2008), On the elastic moduli of three-dimensional assemblies of spheres: Characterization and modeling of fluctuations in the particle displacement and rotation, *Int. J. Solids Struct.*, *45*, 1101–1123.

Arzt, E. (1982), The influence of an increasing particle coordination on the densification of spherical powders, *Acta Metall.*, *30*, 1883–1890.

Bernabé, Y., and B. Evans (2007), Numerical modeling of pressure solution deformation at axisymmetric asperities under normal load, in *Rock Physics and Geomechanics in the Study of Reservoirs and Repositories*, edited by C. David and M. Le Ravalec-Dupin, pp. 185–205, Geol. Soc., London.

Bernabé, Y., B. Evans, and D. D. Fitzenz (2009), Stress transfer during pressure solution compression of rigidly coupled axisymmetric asperities pressed against a flat semi-infinite solid, *Pure Appl. Geophys.*, *166*, 1–27.

Blanpied, M. L., D. A. Lockner, and J. D. Byerlee (1992), An earthquake mechanism based on rapid sealing of faults, *Nature*, *358*, 574–576.

Boutt, D. F., B. K. Cook, B. J. O. L. McPherson, and J. R. Williams (2007), Direct simulation of fluid-solid mechanics in porous media using the discrete element and lattice-Boltzmann methods, *J. Geophys. Res.*, *112*, B10209, doi:10.1029/2004JB003213.

Bruno, M. S., and R. B. Nelson (1991), Microstructural analysis of the inelastic behavior of sedimentary rock, *Mech. Mater.*, *12*, 95–118.

Chester, J. S., S. C. Lenz, F. M. Chester, and R. A. Lang (2004), Mechanisms of compaction of quartz sand at diagenetic conditions, *Earth Planet. Sci. Lett.*, *220*, 435–451.

Chester, F. M., J. S. Chester, A. K. Kronenberg, and A. Hajash (2007), Subcritical creep compaction of quartz sand at diagenetic conditions: Effects of water and grain size, *J. Geophys. Res.*, *112*, B06203, doi:10.1029/2006JB004317.

Cox, S. F., and M. S. Paterson (1991), Experimental dissolution-precipitation creep in quartz aggregates at high temperatures, *Geophys. Res. Lett.*, *18*, 1401–1404, doi:10.1029/91GL01802.

Cundall, P. A., and O. D. L. Strack (1979), A discrete numerical model for granular assemblies, *Geotechnique*, *29*, 47–65.

den Brok, S. W. J. (1998), Effect of microcracking on pressure-solution strain rate: The Gratz grain-boundary model, *Geology*, *26*, 915–918.

de Meer, S., C. J. Spiers, C. J. Peach, and T. Watanabe (2002), Diffusive properties of fluid-filled grain boundaries measured electrically during active pressure solution, *Earth Planet. Sci. Lett.*, *200*, 147–157.

de Meer, S., C. J. Spiers, and S. Nakashima (2005), Structure and diffusive properties of fluid-filled grain boundaries: An in-situ study using infrared (micro) spectroscopy, *Earth Planet. Sci. Lett.*, *232*, 403–414.

Digby, P. J. (1981), The effective elastic moduli of porous granular rocks, *J. Appl. Mech.*, *48*, 803–808.

Domenico, S. N. (1977), Elastic properties of unconsolidated porous sand reservoirs, *Geophysics*, *42*, 1339–1368.

Dutta, T., G. Mavko, and T. Mukerji (2010), Improved granular medium model for unconsolidated sands using coordination number, porosity, and pressure relations, *Geophysics*, *75*, E91–E99.

Dysthe, D. K., Y. Podladchikov, F. Renard, J. Feder, and B. Jamtveit (2002), Universal scaling in transient creep, *Phys. Rev. Lett.*, *89*, doi:10.1103/PhysRevLett.89.246102.

Dysthe, D. K., F. Renard, J. Feder, B. Jamtveit, P. Meakin, and T. Jøssang (2003), High-resolution measurements of pressure solution, *Phys. Rev. E*, *68*, 011,603.

Ehrenberg, S. N., P. H. Nadeau, and Ø. Steen (2009), Petroleum reservoir porosity versus depth: Influence of geological age, *Am. Assoc. Pet. Geol. Bull.*, *93*, 1281–1296.

Elata, D., and J. G. Berryman (1996), Contact force-displacement laws and the mechanical behavior of random packs of identical spheres, *Mech. Mater.*, *24*, 229–240.

Elliot, D. (1973), Diffusion flow law in metamorphic rocks, *Bull. Geol. Soc. Am.*, *84*, 2645–2664.

Fischmeister, H. F., E. Arzt, and L. R. Olsson (1978), Particle deformation and sliding during compaction of spherical powders: A study by quantitative metallography, *Powder Metall.*, *4*, 179–187.

Fitzenz, D. D., A. Jalobeanu, and S. H. Hickman (2007), Integrating laboratory creep data with numerical fault models: A Bayesian framework, *J. Geophys. Res.*, *112*, B08410, doi:10.1029/02006JB004792.

Ghoussoub, J., and Y. M. Leroy (2001), Solid-fluid phase transformation within grain boundaries during compaction by pressure solution, *J. Mech. Phys. Solids*, *49*, 2385–2430.

Gong, G. (2008), DEM simulations of drained and undrained behaviour, PhD thesis, 211 pp., University of Birmingham, U. K.

Gratier, J.-P. (1987), Pressure solution-deposition creep and associated tectonic differentiation in sedimentary rocks, in *Deformation of Sediments and Sedimentary Rocks*, *Special Pub.*, vol. 29, edited by M. E. Jones and R. M. F. Preston, pp. 25–38, Geological Society, London.

Gratier, J.-P. (1993), Experimental pressure solution of halite by an indenter technique, *Geophys. Res. Lett.*, *20*, 1647–1650, doi:10.1029/93GL01398.

Gratier, J.-P., R. Guiguet, F. Renard, L. Jenatton, and D. Bernard (2009), A pressure solution creep law for quartz from indentation experiments, *J. Geophys. Res.*, *114*, B03403, doi:10.1029/2008JB005652.

Gratz, A. J. (1991), Solution-transfer compaction of quartzites: Progress toward a rate law, *Geology*, *19*, 901–904.

Harthong, B., J.-F. Jérier, P. Dorémus, D. Imbault, and F.-V. Donzé (2009), Modeling of high-density compaction of granular materials by the discrete element method, *Int. J. Solids Struct.*, *46*, 3357–3364.

Hickman, S. H., and B. Evans (1991), Experimental pressure solution in halite: The effect of grain/interphase boundary structure, *J. Geol. Soc. London*, *148*, 549–560.

Hickman, S. H., and B. Evans (1992), Growth of grain contacts in halite by solution transfer: Implications for diagenesis, lithification, and strength recovery, in *Fault Mechanics and Transport Properties of Rocks*, edited by B. Evans and T.-F. Wong, pp. 253–280, Academic Press, San Diego, Calif.

Hickman, S. H., and B. Evans (1995), Kinetics of pressure solution at halite-silica interfaces and intergranular clay films, *J. Geophys. Res.*, *100*, 13,113–13,132, doi:10.1029/95JB00911.

Holtzman, R. (2012), Micromechanical model of weakly-cemented sediments, *Int. J. Numer. Anal. Methods Geomech.*, *36*, 944–958.

Karcz, Z., E. Aharonov, D. Ertas, R. Polizzotti, and C. H. Scholz (2006), Stability of a sodium chloride indenter contact undergoing pressure solution, *Geology*, *34*, 61–63.

Karcz, Z., E. Aharonov, D. Ertas, R. Polizzotti, and C. H. Scholz (2008), Deformation by dissolution and plastic flow of a single crystal sodium chloride indenter: An experimental study under the confocal microscope, *J. Geophys. Res.*, *113*, B04205, doi:10.1029/2006JB004630.

Karner, S. L., F. M. Chester, A. K. Kronenberg, and J. S. Chester (2003), Subcritical compaction and yielding of granular quartz sand, *Tectonophysics*, *377*, 357–381.
Lehner, F. K. (1990), Thermodynamics of rock deformation by pressure solution, in *Deformation Processes in Minerals, Ceramics and Rocks*, *Mineral. Soc. Series*, vol. 1, edited by D. J. Barber and P. G. Meredith, pp. 296–333, Springer, Netherlands.
Lehner, F. K. (1995), A model for intergranular pressure solution in open systems, *Tectonophysics*, *245*, 153–170.
Lehner, F. K., and J. Bataille (1984/1985), Nonequilibrium thermodynamics of pressure solution, *Pure Appl. Geophys.*, *122*, 53–85.
Lehner, F. K., and Y. Leroy (2004), Sandstone compaction by intergranular pressure solution, in *Mech. Fluid-Saturated Rocks*, edited by Y. Guéguen and M. Boutéca, pp. 115–168, Elsevier Academic Press, New York.
Mair, K., and S. Abe (2008), 3D numerical simulations of fault gouge evolution during shear: Grain size reduction and strain localization, *Earth Planet. Sci. Lett.*, *274*, 72–81.
Makse, H. A., N. Gland, D. L. Johnson, and L. M. Schwartz (1999), Why effective medium theory fails in granular materials, *Phys. Rev. Lett.*, *83*, 5070–5073.
Makse, H. A., N. Gland, D. L. Johnson, and L. M. Schwartz (2004), Granular packings: Nonlinear elasticity, sound propagation, and collective relaxation dynamics, *Phys. Rev. E*, *70*, 061302.
Martin, C. L., D. Bouvard, and S. Shima (2003), Study of particle rearrangement during powder compaction by the discrete element method, *J. Mech. Phys. Solids*, *51*, 667–693.
Niemeijer, A., C. J. Spiers, and B. Bos (2002), Compaction creep of quartz sand at 400–600°C: Experimental evidence for dissolution-controlled pressure solution, *Earth Planet. Sci. Lett.*, *195*, 261–275.
Niemeijer, A., D. Elsworth, and C. Marone (2009), Significant effect of grain size distribution on compaction rates in granular aggregates, *Earth Planet. Sci. Lett.*, *284*, 386–391.
Norris, A. N., and D. L. Johnson (1997), Nonlinear elasticity of granular media, *J. Appl. Mech.*, *64*, 39–49.
Paterson, M. S. (1973), Nonhydrostatic thermodynamics and its geologic applications, *Rev. Geophys. Space Phys.*, *11*, 355–389.
Paterson, M. S. (1995), A theory for granular flow accommodated by material transfer via an intergranular fluid, *Tectonophysics*, *245*, 135–151.
Raj, R. (1982), Creep in polycrystalline aggregates by matter transport through a liquid phase, *J. Geophys. Res.*, *87*, 4731–4739, doi:10.1029/JB087iB06p04731.
Renard, F., and P. Ortoleva (1997), Water films at grain-grain contacts: Debye-Hückel osmotic model of stress, salinity, and mineralogy dependence, *Geochim. Cosmochim. Acta*, *61*, 1963–1970.
Renard, F., E. Brosse, and J. P. Gratier (2000), The different processes involved in the mechanism of pressure solution in quartz-rich rocks and their interactions, in *Quartz Cement in Oil Field Sandstones*, *Int. Assoc. Sediment. Spec. Publ.*, vol. 29, edited by R. Worden and S. Morad, pp. 67–78, Blackwell, Oxford, U. K.
Renard, F., D. K. Dysthe, J. Feder, K. Bjørlykke, and B. Jamtveit (2001), Enhanced pressure solution creep rates induced by clay particles: Experimental evidence in salt aggregates, *Geophys. Res. Lett.*, *28*, 1295–1298, doi:10.1029/2000GL012394.
Revil, A. (1999), Pervasive pressure-solution transfer: A poro-visco-plastic model, *Geophys. Res. Lett.*, *26*, 255–258, doi:10.1029/1998GL900268.
Revil, A. (2001), Pervasive pressure solution transfer in a quartz sand, *J. Geophys. Res.*, *106*, 8665–8686, doi:10.1029/2000JB900465.
Revil, A., P. Leroy, A. Ghorbani, N. Florsch, and A. R. Niemeijer (2006), Compaction of quartz sands by pressure solution using a Cole-Cole distribution of relaxation times, *J. Geophys. Res.*, *111*, B09205, doi:10.1029/2005JB004151.
Rothenburg, L., and N. P. Kruyt (2004), Critical state and evolution of coordination number in simulated granular materials, *Int. J. Solids Struct.*, *41*, 5763–5774.
Roux, J.-N. (2000), Geometric origin of mechanical properties of granular materials, *Phys. Rev. E*, *61*, 6802–6836.
Rutter, E. H. (1976), The kinetics of rock deformation by pressure solution, *Philos. Trans. R. Soc. London, Ser. A*, *283*, 203–219.
Rutter, E. H. (1983), Pressure solution in nature, theory and experiment, *J. Geophys. Soc. London*, *140*, 725–740.
Rutter, E. H., and P. H. Wanten (2000), Experimental study of the compaction of phyllosilicate-bearing sand at elevated temperature and with controlled pore water pressure, *J. Sediment. Res.*, *70*, 107–116.
Schutjens, P. M. T. M. (1991), Experimental compaction of quartz sand at low effective stress and temperature conditions, *J. Geol. Soc. London*, *148*, 527–539.
Segall, P., and J. R. Rice (1995), Dilatancy, compaction, and slip instability of a fluid infiltrated fault, *J. Geophys. Res.*, *100*, 122,155–122,171.
Spiers, C. J., P. M. T. M. Schutjens, R. H. Brzesowsky, C. J. Peach, J. L. Liezenberg, and H. J. Zwart (1990), Experimental determination of constitutive parameters governing creep of rocksalt by pressure solution, in *Deformation Mechanisms, Rheology and Tectonics*, *Spec. Pub.*, vol. 54, edited by R. J. Knipe and E. H. Rutter, pp. 215–227, Geological Society, London.
Tada, R., and R. Siever (1986), Experimental knife-edge pressure solution of halite, *Geochim. Cosmochim. Acta*, *50*, 29–36.
Tada, R., and R. Siever (1989), Pressure solution during diagenesis, *Annu. Rev. Earth Planet. Sci.*, *17*, 89–118.
Taron, J., and D. Elsworth (2010), Constraints on compaction rate and equilibrium in the pressure solution creep of quartz aggregates and fractures: Controls of aqueous concentration, *J. Geophys. Res.*, *115*, B07211, doi:10.1029/2009JB007118.
Uri, L., T. Walmann, L. Alberts, D. G. Dysthe, and J. Feder (2006), Structure of plastically compacting granular packings, *Phys. Rev. E*, *73*, doi:10.1103/PhysRevE.73.051301.
Van Noort, R., C. J. Spiers, and G. M. Pennock (2008), Compaction of granular quartz under hydrothermal conditions: Controlling mechanisms and grain boundary processes, *J. Geophys. Res.*, *113*, B12206, doi:10.1029/2008JB005815.
Visser, H. J. M., C. J. Spiers, and S. J. T. Hangx (2012), Effects of interfacial energy on compaction creep by intergranular pressure solution: Theory versus experiments on a rock analog ($NaNO_3$), *J. Geophys. Res.*, *117*, B11211, doi:10.1029/2012JB009590.
Weyl, P. K. (1959), Pressure solution and the force of crystallization: A phenomenological theory, *J. Geophys. Res.*, *78*, 2001–2025, doi:10.1029/JZ064i011p02001.
Zubtsov, S., F. Renard, J.-P. Gratier, R. Guiguet, D. K. Dysthe, and V. Traskine (2004), Experimental pressure solution compaction of synthetic halite/calcite aggregates, *Tectonophysics*, *385*, 45–57.